RSC Advances

PAPER

View Article Online
View Journal | View Issue

Open Access Article. Published on 11 December 2025. Downloaded on 3/15/2026 8:19:21 PM.
This article is licensed under a Creative Commons Attribution-NonCommercial 3.0 Unported Licence.

Check for updates

Cite this: *RSC Adv.*, 2025, **15**, 49474

Interleaving-twisted nanoarchitectured porous organic polymer synergizes photoactivity enhancement and nanozyme-powered microenvironment remodeling for advanced infected wound therapy

Meiyun Du,†[ab] Zongpeng Zhang,†[d] Feng Gao,†[c] Yonglei Qin,*[b] Fei Gao*[a] and Peng Sun*[c]

While systemic antibiotics remain the frontline defense against bacterial infections, the global antimicrobial resistance crisis urgently demands non-inducible therapeutic alternatives. Despite the inherent ability of phototherapy to bypass resistance, its efficacy in state-of-the-art porphyrin-based photosensitizers (PSs) is critically limited by aggregation-caused quenching (ACQ) of photoactivity. To overcome this dual challenge, we designed a conformation-adaptive porous organic polymer (DFP-POP). Featuring a spatially interleaving-twisting molecular architecture achieved by linking triazine–porphyrin units (H_2TDPP, featuring eight amino groups) *via* Schiff-base polymerization with acetyl-rich bridging ferrocene (possessing a sandwich-staggered structure), DFP-POP synergizes three antimicrobial modalities to realize a cascade mechanism. This unique 3D twisted conformation inherently suppresses ACQ by preventing π–π stacking. It simultaneously facilitates broad-spectrum light absorption through extended conjugation and enables multimodal bioactivity *via* ferrocene-mediated enzyme-mimetic catalysis. DFP-POP orchestrates a self-enhanced multimodal therapy by manipulating oxygen in the infected microenvironment (IME). Its catalase-like (CAT-like) activity converts endogenous H_2O_2 to O_2, alleviating hypoxia to enable self-sustaining photodynamic therapy (PDT). Additionally, its pH-responsive peroxidase-like (POD-like) activity precisely generates bactericidal $^{\bullet}OH$ specifically within the weakly acidic IME. Consequently, DFP-POP operates through a synergistic cascade characterized by photothermal membrane disruption, hypoxia-alleviated $^1O_2$ production, and enzyme-amplified $^{\bullet}OH$ generation. In murine wound models, DFP-POP treatment achieved near-complete epithelialization by day 9, significantly outperforming controls. This work pioneers the integration of molecular conformation engineering with microenvironment-responsive catalytic cascades in porous organic polymer design, establishing a new paradigm for combating drug-resistant infections. The synergy between physical phototherapy and biochemical catalysis provides a blueprint for developing advanced smart therapeutic materials.

Received 22nd September 2025
Accepted 3rd December 2025

DOI: 10.1039/d5ra07169k

rsc.li/rsc-advances

Introduction

Infection-related diseases, particularly those caused by bacteria, represent an ever-growing global challenge, posing a serious threat to public health.[1–3] Among these, open infected wounds are notable for their high incidence rate, healing complexity, and association with millions of deaths annually.[4–6] Unlike healthy tissues, infection sites feature a unique pathological microenvironment characterized by hypoxia, elevated peroxide levels, and weak acidity. This microenvironment fosters disease progression, leading to normal cell death and significantly impeding the wound healing process.[7–9] Compounding this problem, the prevalence of drug-resistant bacteria undermines conventional antibiotic therapy, further complicating treatment efforts.[10] Consequently, the development of antibiotic-free antibacterial agents capable of simultaneously exploiting and regulating this infectious microenvironment has become a critical new direction in infection treatment.[11]

[a]*Affiliated Hospital of Shandong Second Medical University, Shandong Second Medical University, Weifang 261053, Shandong, PR China*

[b]*Weifang Mental Health Center, Weifang 261000, Shandong, PR China*

[c]*School of Pharmacy, Shandong Second Medical University, Weifang 261053, Shandong, PR China. E-mail: pengs1993@sdsmu.edu.cn*

[d]*Weifang Hospital of Traditional Chinese Medicine, Shandong Second Medical University, Weifang 261041, Shandong, PR China*

† These authors contribute equal to this work.

© 2025 The Author(s). Published by the Royal Society of Chemistry

Open Access Article. Published on 11 December 2025. Downloaded on 3/15/2026 8:19:21 PM. This article is licensed under a Creative Commons Attribution-NonCommercial 3.0 Unported Licence.

Phototherapy, which exerts therapeutic effects through photosensitizers (PSs) activated by laser irradiation, has emerged as a promising antibiotic-free strategy for bacterial infection therapy.[12] Photothermal therapy (PTT), relying on localized hyperthermia to combat bacteria, has been extensively investigated as a noninvasive antibacterial approach.[13] However, effective bacterial elimination often requires temperatures high enough to cause collateral damage to healthy cells. Photodynamic therapy (PDT) is an O_2-dependent sterilization method that transforms surrounding O_2 into toxic reactive oxygen species (ROS) under laser irradiation to kill bacterial strains.[14] Yet, the intrinsic hypoxia characteristic of bacteria-infected wounds critically limits PDT efficacy.[15] Furthermore, as a PS-dependent modality, the therapeutic outcome of PDT is highly contingent upon the PS properties. For instance, porphyrin-based PSs suffer from self-quenching of photoactivity induced by π–π stacking aggregation. Current research, therefore, focuses on the rational design of PS structures aimed at maximizing photoactivity while effectively mitigating activity quenching.

Artificial enzymes, exhibiting catalytic activity analogous to natural enzymes, are increasingly explored as antibacterial agents with lesion microenvironment-specific responsiveness.[16–19] For example, peroxidase (POD)-mimicking enzymes convert overexpressed hydrogen peroxide (H_2O_2) into highly toxic hydroxyl radicals ($^{\bullet}OH$) within the acidic infectious microenvironment (IME), achieving potent antibacterial activity.[17] Similarly, catalase (CAT)-like enzymes catalyze H_2O_2 decomposition to generate abundant O_2. This action not only alleviates tissue hypoxia at infection sites but also replenishes O_2 for PDT, thereby accelerating the healing of infected wounds.[18] Importantly, enzymatic therapy demonstrates excellent compatibility with other treatment modalities, enabling synergistic and amplified therapeutic outcomes.[19] Nevertheless, engineering diverse therapeutic functions into a single antibacterial agent to achieve the desired efficacy remains challenging.

Porous organic polymers (POPs) constitute a class of emerging artificial multifunctional materials with customizable physicochemical properties, assembled *via* stable covalent linkages from organic building blocks.[20–22] To date, structurally diverse POPs have been successfully developed, demonstrating significant application potential in fields ranging from environmental remediation to biomedical science.[23–25] Among them, conjugated microporous polymers (CMPs), featuring fully conjugated skeleton structures, offer distinct advantages as phototherapeutic PSs.[26] As macromolecular antibacterial agents, POPs effectively circumvent the aggregation-induced self-quenching that plagues conjugated small-molecule PSs, substantially enhancing photoresponsiveness.[27] Furthermore, their unique composition, akin to biomacromolecules, imparts inherent biocompatibility.[28] This structural and functional tailorability renders POPs an ideal platform for synergistic therapy.[29]

Herein, we employ a spatial interleaving and twisting strategy to develop an imine-bonded POP-based antibacterial agent. This involves structural regulation of bridging monomers reacted with the spatial twisted triazine–porphyrin unit (H_2TDPP). The activity of material is effectively controlled by adjusting the bridging monomers. Specifically, DFP-POP utilizes redox-active diacetyl ferrocene (DF) with a sandwich structure as the bridging molecule, serving as a potent photoresponsive therapeutic agent. DFP-POP not only capitalizes on but also actively modulates the IME, thereby accelerating infected wound healing. The incorporation of porphyrin-bearing units into the extended conjugated skeleton confers PDT and PTT capabilities, enhanced by the conjugated backbone. The unique spatial interleaving and twisting conformation maximizes photoactivity while effectively mitigating activity quenching caused by severe π–π stacking aggregation. Repetitive ferrocene units endow CAT-like and POD-like enzymatic activities. This catalyzes the transformation of overexpressed endogenous peroxide (H_2O_2) into O_2 and toxic $^{\bullet}OH$ specifically at the lesion site. DFP-POP simultaneously eradicates infection, alleviates hypoxia, and rebalances key factors within the infectious microenvironment. Consequently, DFP-POP features self-enhanced photothermal, photodynamic, and dual enzyme-mimetic activities. It functions as a synergistic antimicrobial platform that establishes a microenvironment conducive to cell proliferation, significantly accelerating wound healing.

Results and discussions

Scheme 1 illustrated the typical synthesis route for imine-bonded POPs. This involved reacting 5,10,15,20-tetrakis(4-(2,4-diaminotriazine)phenyl)porphyrin (H_2TDPP)-containing eight amino groups with multifunctional acetyl-containing monomers, including 1,1′-diacetylferrocene (DF), 1,3,5-tris(4-acetylphenyl)benzene (TAPB), 4′,4″(5″)-diacetyldibenzo-18-crown-6 (DABC), and tetra(4-acetylphenyl)methane (TAPM), *via* a cost-effective Schiff base reaction.[30] The resulting POPs were denoted according to the bridging monomer used, namely DFP-POP (DF), TAPBP-POP (TAPB), DABCP-POP (DABC), and TAPMP-POP (TAPM). For instance, DFP-POP was synthesized by reacting H_2TDPP with diacetylferrocene at 180 °C for 72 h. The resulting polymer was then washed sequentially with methanol, THF, and dichloromethane, followed by vacuum drying at 80 °C for 12 h. Detailed synthesis procedures for the monomers (H_2TDPP, DF, TAPB, DABC, TAPM) and the characterization data for all POP products (DFP-POP, TAPBP-POP, DABCP-POP, TAPMP-POP) are provided in the SI (Fig. S1–S5).

To confirm the successful formation of porous networks Fourier transform infrared spectroscopy (FTIR; Fig. 1a and S6) analysis was initially conducted.[31] As shown, characteristic absorption bands corresponding to the C=O stretching vibration (~1660 cm^{-1}) of the acetyl-containing monomers and the amine feature (~3190 cm^{-1}) attributed to the triazine units significantly weakened or even disappeared after polymerization.[32,33] Concurrently, intense peaks emerged at ~1580 cm^{-1}, assigned to the C=N stretching vibration of imine bonds, confirming successful polymerization of the monomers.[32] Solid-state ^{13}C cross-polarization magic-angle spinning nuclear magnetic resonance (^{13}C NMR; Fig. 1b) spectroscopy of DFP-

Open Access Article. Published on 11 December 2025. Downloaded on 3/15/2026 8:19:21 PM.
This article is licensed under a Creative Commons Attribution-NonCommercial 3.0 Unported Licence.

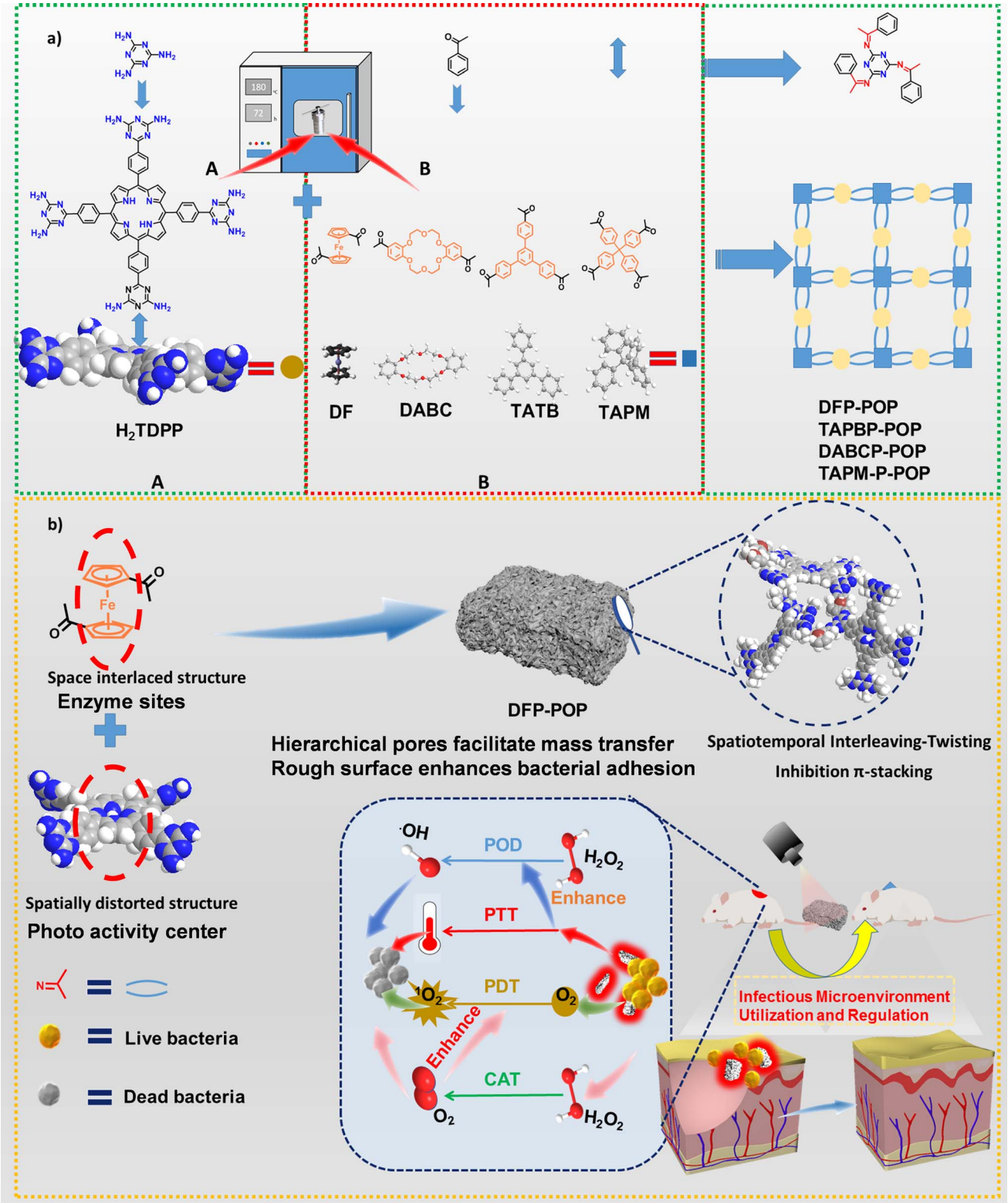

Scheme 1 (a) Route for the synthesis of POPs from poly-acetylated monomers; (b) mechanism of DFP-POP for the accelerating of infectious wounds.

POP exhibited broad carbon signals spanning 10–180 ppm. Signals within the 143–170 ppm region corresponded to aromatic carbons in the triazine rings and the imine carbon atoms of the porphyrin structure.[34] The remaining signals at 16 ppm and 54 ppm were assigned to the methyl groups and the ferrocene metallocene ring, respectively.[35]

 © 2025 The Author(s). Published by the Royal Society of Chemistry

Open Access Article. Published on 11 December 2025. Downloaded on 3/15/2026 8:19:21 PM.
This article is licensed under a Creative Commons Attribution-NonCommercial 3.0 Unported Licence.

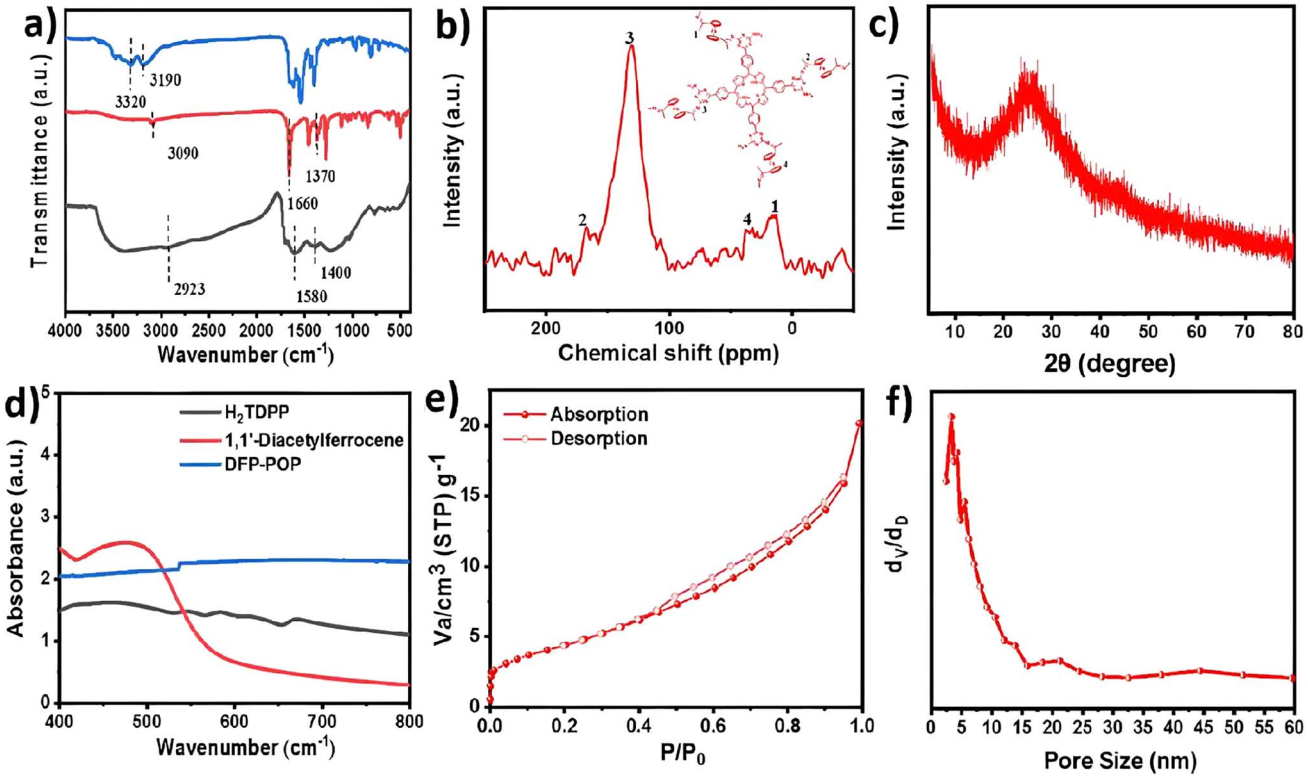

Fig. 1 Physical characterization of DFP-POP. (a) The FT-IR spectra of the reactive monomers and polymers; (b) solid state ^{13}C NMR spectrum of DFP-POP; (c) powder XRD of DFP-POP; (d) the UV absorption of DFC, H_2TDPP and DFP-POP in water; (e) low temperature N_2 absorption–desorption isotherm of DFP-POP at 77 K; (f) pore size distribution curves of DFP-POP.

Thermogravimetric analysis (TGA; Fig. S7) assessed the thermal stability of DFP-POP under N_2. An initial weight loss below 100 °C is attributed to the desorption of physisorbed water from the highly polar porous framework.[36] Remarkably, DFP-POP retained over 50% of its weight even at 800 °C, demonstrating excellent thermal stability.[37] Fig. 1d displayed the powder X-ray diffraction (PXRD) of DFP-POP. As seen, similar to the previous reports, DFP-POP only presented a broad peak around 25°, reflecting its amorphous nature.[38] Low-temperature N_2 sorption analysis was employed to assess the porosity of DFP-POP (Fig. 1e). As seen, the isotherm displayed type IV behavior featuring a distinct hysteresis loop in the adsorption–desorption branches with a steep nitrogen uptake at low relative pressures ($P/P_0 < 0.01$) These characteristics indicated a hierarchical pore structure of DFP-POP containing both micropores and mesopores.[39] The Brunauer–Emmett–Teller (BET) surface area was calculated as 16.5 $m^2\ g^{-1}$, with a total pore volume of 0.031 $cm^3\ g^{-1}$. Pore size distribution (PSD) analysis derived from non-local density functional theory (NLDFT) modeling (Fig. 1f) revealed a primary micropore peak at 0.61 nm, with secondary maxima at 0.76 nm and 0.88 nm.

The morphology and microstructure of DFP-POP were comprehensively characterized by scanning and transmission electron microscopy (SEM/TEM). The SEM images revealed a uniform coralline-shaped architecture comprising intergrown nanoparticles that form interconnected macropores throughout the polymer matrix (Fig. 2a–c). Corresponding TEM images (Fig. 2d–g) confirmed the hierarchical porosity, with homogeneously dispersed micropores clearly visible as bright/dark field contrast variations. As expected, the energy-dispersive X-ray spectroscopy (EDX, Fig. S8) and elemental mapping (Fig. 2h–k) demonstrate homogeneous distribution of Fe (6.29 wt%), N (6.09 wt%), and the predominant C (87.62 wt%) throughout the hierarchical porous matrix.

The photophysical properties of DFP-POP were evaluated through comprehensive optical characterization. The UV-vis-NIR absorption spectrum (Fig. S9) revealed broad absorption spanning 400–800 nm, featuring an intense peak at 450 nm characteristic of porphyrin units, confirming its potential as a phototherapeutic agent.[40] The photothermal conversion capability of DFP-POP was systematically investigated under varying concentrations (Fig. 3a–c) and laser power densities (Fig. 3d).[41] The temperature increase (ΔT) exhibited pronounced concentration dependence, rising from 16.4 °C (100 μg mL^{-1}) to 38.7 °C (500 μg mL^{-1}) under 638 nm irradiation (1.0 W cm^{-2}, 10 min). By contrast, pure water displayed negligible heating ($\Delta T =$ 0.5 °C) under identical conditions. Thermal imaging confirmed this concentration-dependent warming behavior through observable pseudo-color progression.[42] Power-dependent studies demonstrated significant enhancement in photothermal response with the increasing the irradiance from 0.5 to 2.0 W cm^{-2} elevated ΔT from 14.4 °C to 48.4 °C at 400 μg mL^{-1}

Open Access Article. Published on 11 December 2025. Downloaded on 3/15/2026 8:19:21 PM.
This article is licensed under a Creative Commons Attribution-NonCommercial 3.0 Unported Licence.

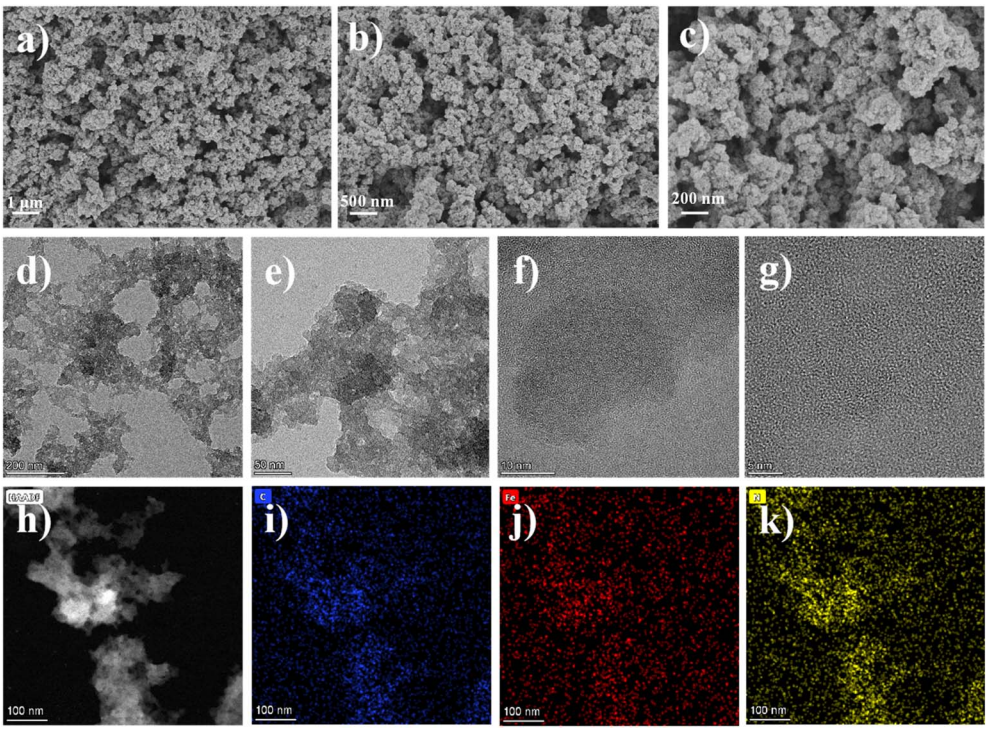

Fig. 2 (a–c) SEM of DFP-POP at scale bars of 1 μm, 500 nm and 200 nm, respectively; (d–g) TEM of DFP-POP at scale bars of 200, 50, 10, and 5 nm, respectively; (h–k) element mappings of DFP-POP at a scale bar of 100 nm.

concentration. Comparative analysis at equivalent concentrations (400 μg mL^{-1}, 638 nm, 1.0 W cm^{-2}, 10 min) revealed photothermal performance comparable to control POPs (TAPBP-POP, DABCP-POP, TAPMP-POP; Fig. S10). Furthermore, DFP-POP exhibited outstanding photothermal stability with negligible efficiency attenuation across five laser on/off cycles (Fig. 3e). Photothermal conversion efficiency (η), calculated using eqn (S1)–(S3) through an independent heating–cooling cycle (Fig. 3f and g), reached 43.98%, exceeding most reported POP-based photothermal agents (Table S1).

Subsequent evaluation of photodynamic and enzyme-mimetic activities revealed the exceptional capabilities of DFP-POP for the generation of ROS. Photodynamic performance was quantified using 1,3-diphenylbenzofuran (DPBF) as a singlet oxygen ($^1O_2$) probe.[43] UV-vis absorption spectra (Fig. 4a) revealed DFP-POP exhibited significantly broader and more intense absorption (300–800 nm) than H_2TDPP and DF monomers in the DMSO. This enhanced photoresponsiveness derived from an extended π-conjugation within the polymer framework. Under laser irradiation (638 nm, 1.0 W cm^{-2}), control experiments showed minimal DPBF decay (420 nm absorbance; Fig. 4b). Strikingly, both porphyrin monomer and DFP-POP induced substantial DPBF degradation under identical conditions, with DFP-POP exhibiting superior kinetics (Fig. 4c and d).

Quantitative analysis (Fig. 4e) confirmed an exceptional $^1O_2$ generation of DFP-POP with 99% DPBF decay within 4 min, dramatically exceeding porphyrin monomer (60%) and background decay (10.38%).[44,45] This rapid ROS generation capability stems from the unique spatially interleaved, twisted architecture of DFP-POP, which maximized photoactivity while mitigating quenching.[46] DFP-POP exhibited excellent photodynamic stability, evidenced by consistent DPBF degradation kinetics across sequential irradiation intervals (2, 4, and 6 min; Fig. 4f). These results confirmed that ferrocene-derived conjugation bridges substantially enhanced ROS production efficiency. The optical chemistry stability of DFP-POP was systematically evaluated under diverse conditions. UV-vis absorption spectra revealed remarkable pH tolerance, with near-identical absorption profiles across acidic to basic media (Fig. S11a). Photothermal cycling stability was demonstrated through the comparison of UV-vis spectrum recorded before and after the five consecutive laser on/off cycles, where only minimal attenuation was detected (Fig. S11b). Long-term storage stability was assessed by monitoring photothermal response after 15-day aqueous immersion. The resulting temperature profile exhibited negligible deviation from the initial response, indicating exceptional water resistance (Fig. S11c). Photodynamic stability was quantified through DPBF degradation assays (420 nm absorption) over 4 days. DFP-POP maintained consistent singlet oxygen ($^1O_2$) generation capacity, with negligible variation in degradation kinetics throughout the testing period (Fig. S11d). These comprehensive analyses confirmed an exceptional stability profile of DFP-POP.

The peroxidase-like (POD-like) activity of DFP-POP was evaluated using 3,3′,5,5′-tetramethylbenzidine (TMB) as an indicator, which underwent a color transition from colorless to blue upon hydroxyl radical ($^{\bullet}OH$) generation.[45] As shown in Fig. 5a, pronounced color change accompanied by significant

 © 2025 The Author(s). Published by the Royal Society of Chemistry

Open Access Article. Published on 11 December 2025. Downloaded on 3/15/2026 8:19:21 PM.
This article is licensed under a Creative Commons Attribution-NonCommercial 3.0 Unported Licence.

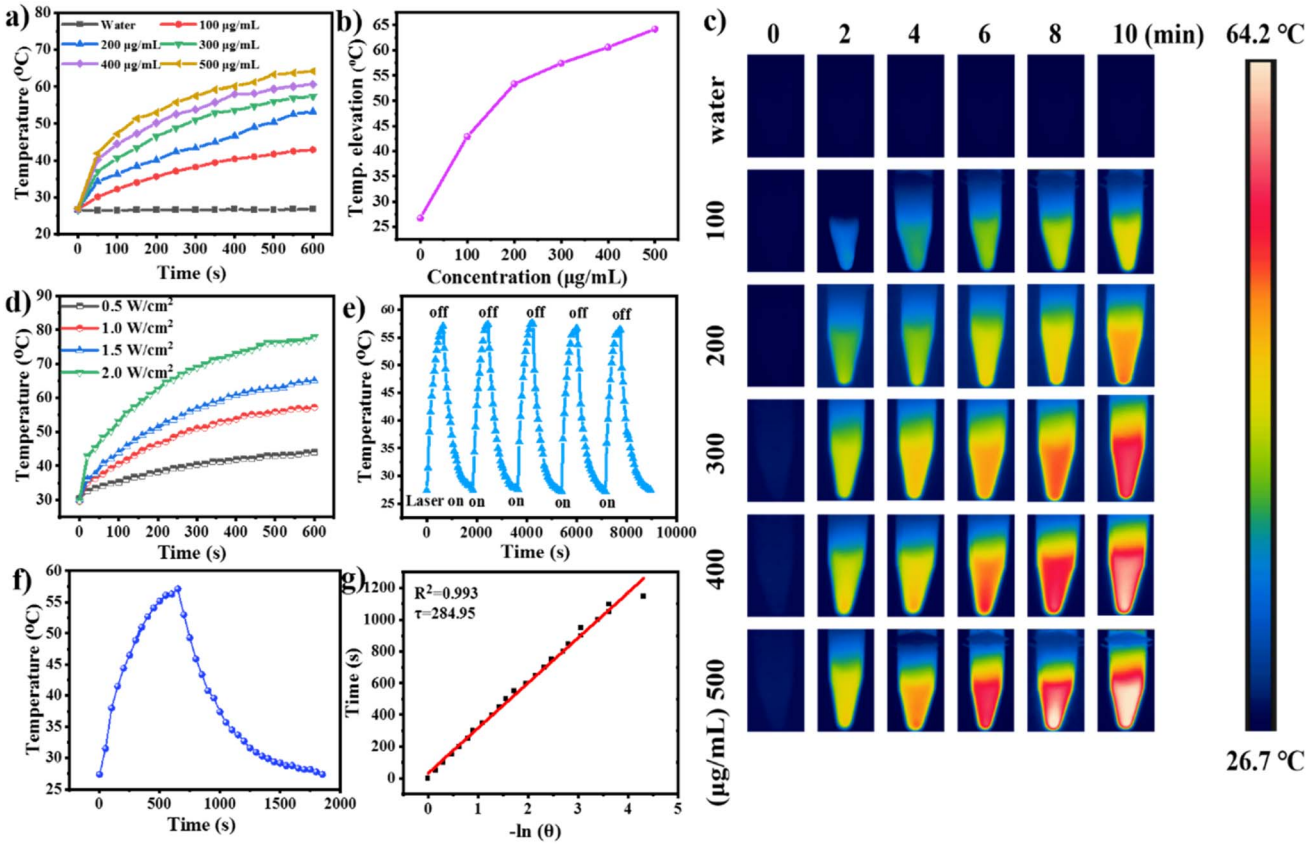

Fig. 3 (a) Temperature rise curves of DFP-POP aqueous suspension at different concentrations under laser irradiation (638 nm, 1 W cm^{-2}); (b) change curve of concentration *versus* temperature after 10 min of laser irradiation; (c) infrared thermal images of different concentrations of DFP-POP at varied time periods; (d) temperature change curves of the DFP-POP (400 μg mL^{-1}) suspension at different power densities. (e) Temperature curve of DFP-POP (400 μg mL^{-1}) under 5 laser on/off cycles; (f) a single temperature cycle curve; (g) negative log of the cooling time and temperature.

UV-vis absorption at 650 nm occurred exclusively in media containing both DFP-POP and H_2O_2. Electron paramagnetic resonance (EPR) spectroscopy confirmed $^{\bullet}OH$ production, exhibiting the characteristic four-peak spectrum of DMPO-$^{\bullet}OH$ adducts (Fig. 5b).[46] Meanwhile, the enzyme-mimetic activity of DFP-POP demonstrated dual dependencies on both the sample concentration and media pH. Specifically, the POD-mimetic activity increased proportionally with DFP-POP concentration. But, the POD-mimetic activity showed a biphasic response to decreasing pH, initially increasing then decreasing. Critically, DFP-POP exhibited substantially enhanced POD-mimetic activity at pH 5.5 (mimicking IME) *versus* negligible activity at pH 6.5 (Fig. 5c and d). This pH-responsive behavior was further augmented by laser irradiation (Fig. S12). Catalase-mimetic (CAT-like) activity was assessed *via* H_2O_2 decomposition monitored at 240 nm.[47] Standard aqueous solutions of H_2O_2 were prepared across a concentration gradient (0–100 mM). UV-vis absorption spectra (Fig. S13) revealed characteristic absorption at ~240 nm with absorbance intensities scaling linearly with H_2O_2 concentration, establishing the quantitative relationship required for subsequent catalase-like activity quantification. Under neutral conditions (pH 7.4), simultaneous presence of DFP-POP and H_2O_2 induced visible oxygen bubbles and progressive decay of H_2O_2 absorption, while H_2O_2 alone showed no reaction (Fig. 5e and f). Notably, DFP-POP maintained comparable CAT-mimetic activity at pH 6.5 (Fig. 5g and h), enabling both hypoxia alleviation and oxygen supply for enhanced PDT at infection sites.

To assess the potential of DFP-POP as a macromolecular antimicrobial agent, we selected *S. aureus* (Gram-positive) and *E. coli* (Gram-negative) as model pathogens (Fig. 6). Dose-dependent bactericidal efficacy was first evaluated under combined H_2O_2 treatment and laser irradiation (Fig. S14). As seen, the bacterial viability decreased significantly with increasing DFP-POP concentration (0–200 μg mL^{-1}), reaching only 3.14% (*S. aureus*) and 0% (*E. coli*) survival at 200 μg mL^{-1}. The heightened susceptibility of *E. coli* was attributed to its distinct cell wall architecture.[48] To illustrate the synergistic bacterial inactivation mechanism, both bacteria underwent different treatments, including the (I) control, (II) H_2O_2, (III) DFP-POP, (IV) DFP-POP + H_2O_2, (V) DFP-POP + laser, (VI) H_2O_2 + laser, (VII) DFP-POP, as well as (VIII) DFP-POP + H_2O_2 group, in which the concentration of DFP-POP was 200 μg mL^{-1}. As displayed in Fig. 6a and c, compared with the control group (with/without laser illumination), the number of viable colonies treated by H_2O_2 was decreased slightly regardless of the laser irradiation, demonstrating the weak bacteriostatic action of H_2O_2. However, the bactericidal efficacy of DFP-POP was

Open Access Article. Published on 11 December 2025. Downloaded on 3/15/2026 8:19:21 PM.
This article is licensed under a Creative Commons Attribution-NonCommercial 3.0 Unported Licence.

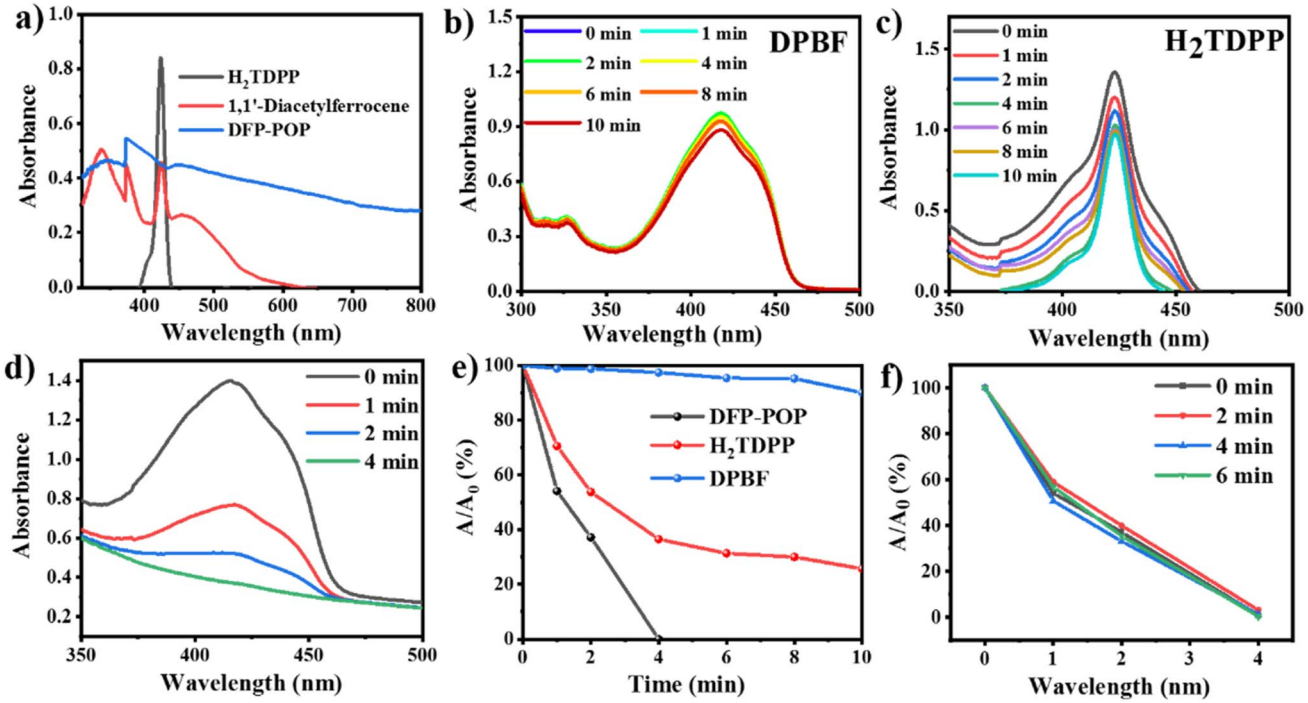

Fig. 4 (a) UV-visible absorption of H_2TDPP, DF and DFP-POP; (b–d) the photodynamic of DPBF, H_2TDPP and DFP-POP under laser irradiation; (e) decay curves of UV absorption by H_2TDPP, DFP-POP and DPBF; (f) UV absorption changes of DPBF at 420 nm in the presence of DFP-POP following various laser irradiation durations (2, 4, and 6 min).

significantly intensified through either H_2O_2 addition or red light exposure. Following H_2O_2 treatment, survival rates decreased to 65.58 ± 3.72% (*S. aureus*) and 67.99 ± 2.29% (*E. coli*), attributable to POD-mimetic catalysis converting H_2O_2 into cytotoxic $^{\bullet}OH$.[49] Under laser irradiation, survival rates plummeted to 3.19 ± 0.21% (*S. aureus*) and 0.48 ± 0.38% (*E. coli*), demonstrating synergistic photothermal–photodynamic action. Critically, the combined treatment (DFP-POP + H_2O_2 + laser) achieved near-total bacterial eradication through PTT/PDT/enzyme cascade synergy, achieving a reduction of 96.81 ± 0.21% and 99.52 ± 0.38% for *S. aureus* and *E. coli*, respectively. Comparative analysis (Fig. S15) confirmed the superiority

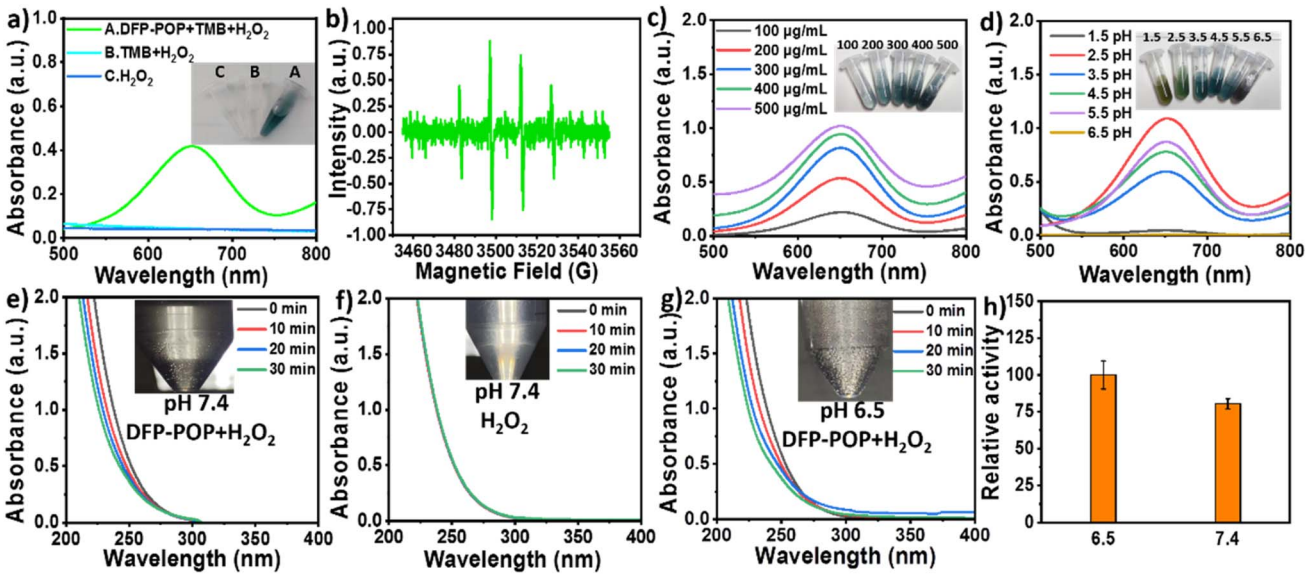

Fig. 5 (a) UV absorption of TMB, TMB + H_2O_2, and DFP-POP + TMB + H_2O_2 around 650 nm; (b) electron paramagnetic resonance of the DFP-POP solution; (c) UV absorption peak at 650 nm for different concentrations of DFP-POP solution at pH 5.5; (d) UV absorption of 500 μg mL^{-1} DFP-POP solution producing $^{\bullet}OH$ in PBS with different pH; (e and f) the degradation curve of H_2O_2 by DFP-POP and H_2O_2 with time measured by UV-vis spectra at pH of 7.4; (g and h) the degradation curve of H_2O_2 by DFP-POP with time at pH of 6.5.

 © 2025 The Author(s). Published by the Royal Society of Chemistry

Open Access Article. Published on 11 December 2025. Downloaded on 3/15/2026 8:19:21 PM.
This article is licensed under a Creative Commons Attribution-NonCommercial 3.0 Unported Licence.

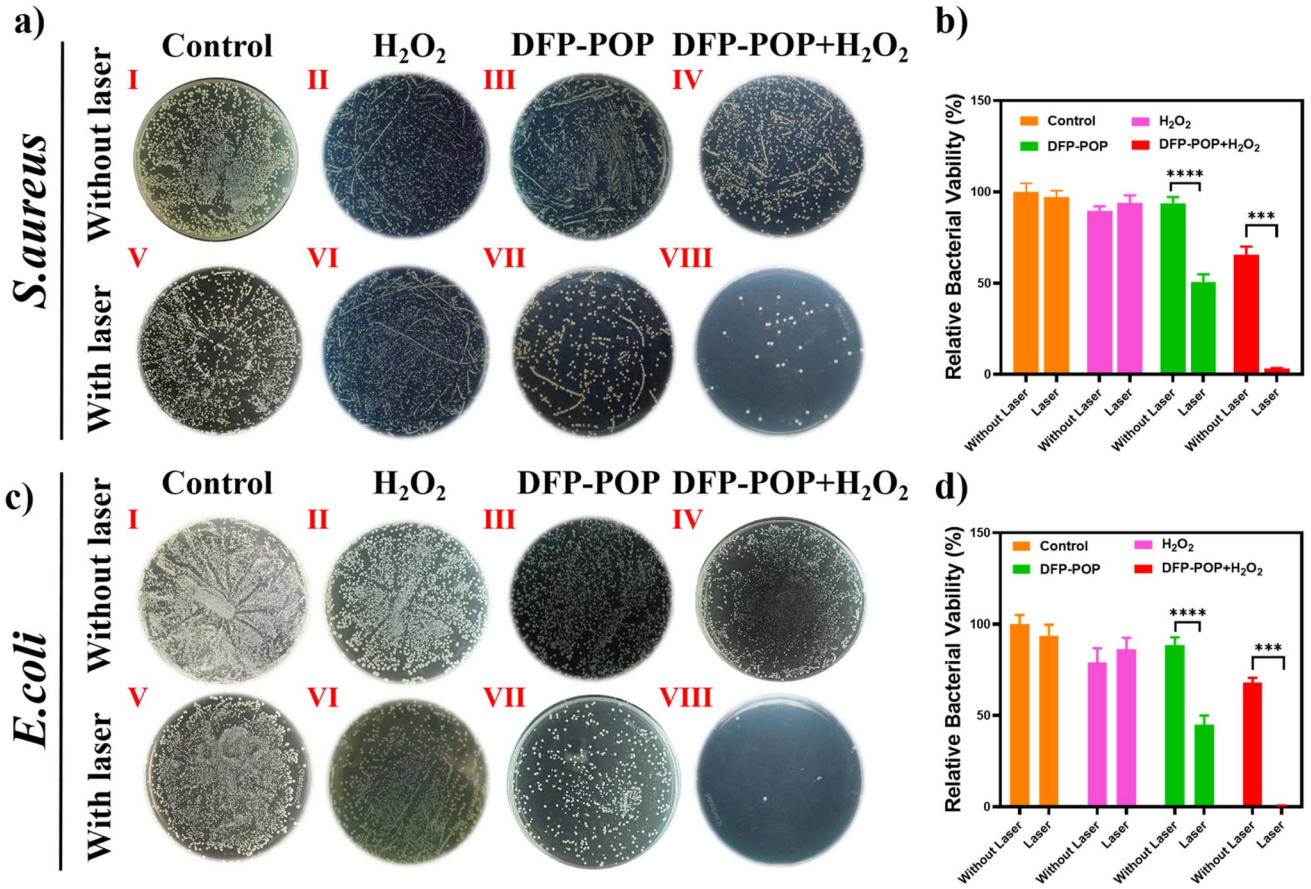

Fig. 6 Colony growth plots of the bacteria in the medium formed by (a) *S. aureus* and (c) *E. coli* treated with (I) PBS, (II) H_2O_2, (III) DFP-POP, (IV) DFP-POP + H_2O_2, (V) PBS + laser, (VI) H_2O_2 + laser, (VII) DFP-POP + laser, (VIII) DFP-POP + H_2O_2 + laser based on plate count method; bar graph of bacterial survival rates of (b) *S. aureus* and (d) *E. coli* treated with different groups. The concentration of DFP-POP and H_2O_2 was 200 μg mL^{-1} and 10 μM, respectively, and the laser power was set as 1.0 W cm^{-2} (638 nm) with an irradiation duration of 10 min. Results are presented as mean ± S.D. (*p < 0.05, **p < 0.01, ***p < 0.001, ****p < 0.0001, analyzed by Student's t-test).

of DFP-POP over structural analogues (DTPMP-POP, DABCP-POP, TAPBP-POP) under identical conditions (200 μg mL^{-1}, H_2O_2, 638 nm laser, 1.0 W cm^{-2}, 10 min). Specifically, DFP-POP achieved >96% bactericidal efficacy at substantially reduced dosages while outperforming most of the recently reported phototherapy agents (Table S2).

To directly visualize synergistic bactericidal effects of DFP-POP, bacterial viability after various treatments was assessed using SYTO 9/propidium iodide (PI) dual staining, where live and dead bacteria fluorescence green and red, respectively.[50] As shown in Fig. 7, aligned with corresponding plate counting results, the PBS (with/without laser), H_2O_2 (with/without laser), and DFP-POP-only treated bacteria exhibited predominant green fluorescence. Conversely, treatment groups involving DFP-POP combined with either H_2O_2 or laser irradiation showed distinct red fluorescence, indicating substantial bacterial death. Critically, bacteria treated with the triple combination (DFP-POP + H_2O_2 + laser) exhibited exclusively red fluorescence, demonstrating near-complete bacterial eradication.

TEM further elucidated bacterial membrane integrity under various treatments (Fig. 7b). Both *S. aureus* and *E. coli* exposed to control solutions or H_2O_2 (with/without laser) maintained smooth surfaces and intact cellular architectures. In contrast, DFP-POP-containing treatment groups (Fig. 7bVI–VIII) exhibited concentration-dependent membrane damage. Specifically, DFP-POP alone caused minimal structural alterations. However, the DFP-POP + laser and DFP-POP + H_2O_2 treatments induced significant membrane wrinkling. Notably, the triple-combination (DFP-POP + H_2O_2 + laser) provoked severe membrane rupture. This progressive structural deterioration, particularly the complete membrane disintegration observed in the synergistic treatment group, directly correlated with accelerated bacterial death, confirming the therapeutic superiority of the photothermal–photodynamic–enzyme cascade mechanism of DFP-POP.

To further verify the potential application *in vivo*, the biocompatibility of DFP-POP was investigated respectively by hemolysis (Fig. 8a), cytotoxicity (Fig. 8b), as well as cell migration assays (Fig. 8c and d).[51] As displayed in Fig. 8a, the hemolysis rate of DFP-POP was slightly increased with the increase of DFP-POP dosage, which was well retained less than 4% in the experimental ranges (100–600 μg mL^{-1}). Cytotoxicity test demonstrated the cell survival rate was maintained well

Open Access Article. Published on 11 December 2025. Downloaded on 3/15/2026 8:19:21 PM.
This article is licensed under a Creative Commons Attribution-NonCommercial 3.0 Unported Licence.

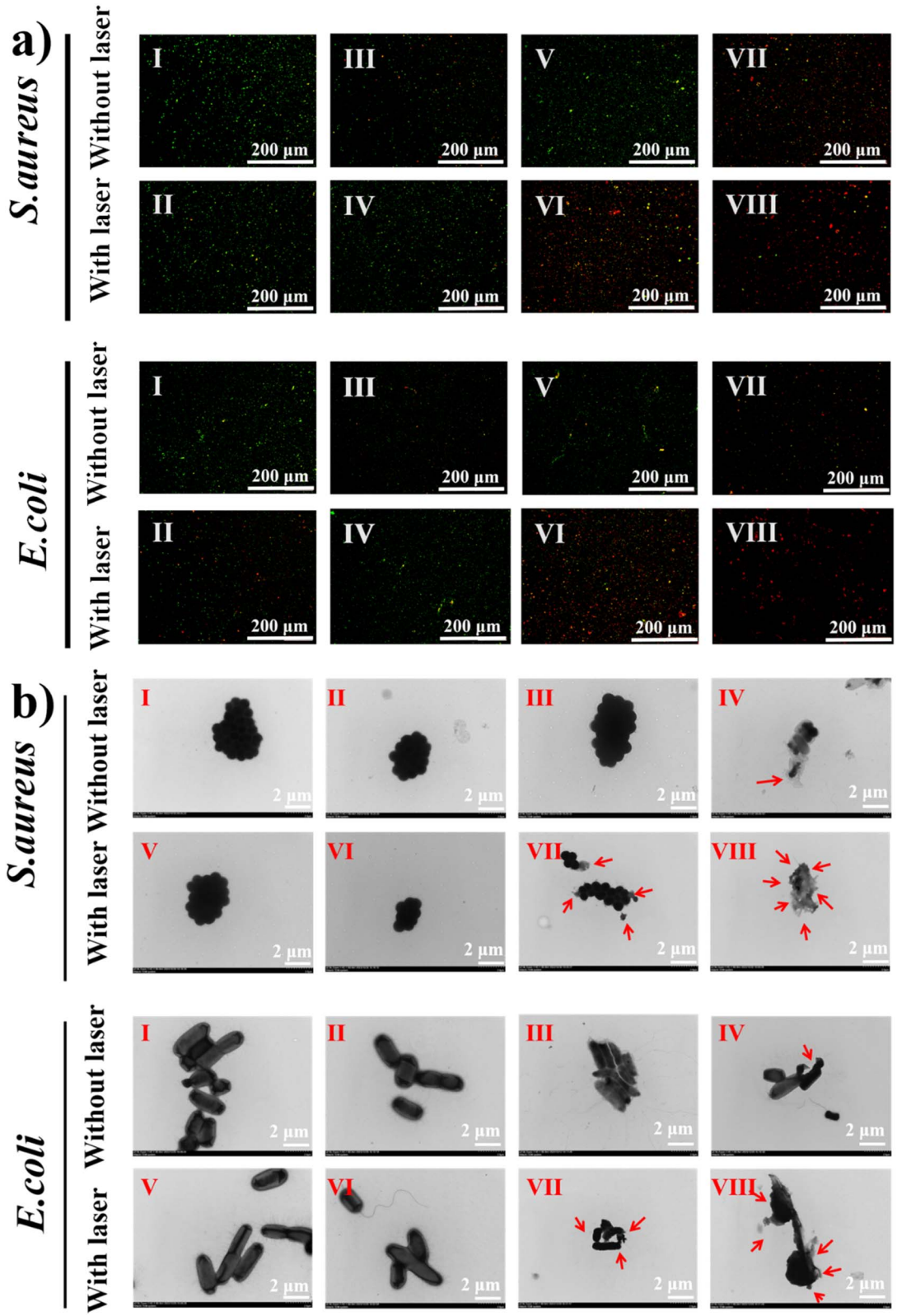

Fig. 7 Fluorescence images of (a) *S. aureus* and *E. coli* and TEM of (b) *S. aureus* and *E. coli* incubated with by (I) PBS, (II) H_2O_2, (III) DFP-POP, (IV) DFP-POP + H_2O_2, (V) PBS + laser, (VI) H_2O_2 + laser, (VII) DFP-POP + laser, (VIII) DFP-POP + H_2O_2 + laser.

above 80% even at the high sample dosage (600 μg mL^{-1}), maintaining ~85% at the therapeutic concentration (200 μg mL^{-1}). Scratch healing showed negligible difference of DFP-POP at varied concentrations from controls after 24/48 h treatment. These results collectively confirmed the exceptional biocompatibility of DFP-POP.

 © 2025 The Author(s). Published by the Royal Society of Chemistry

Open Access Article. Published on 11 December 2025. Downloaded on 3/15/2026 8:19:21 PM.
This article is licensed under a Creative Commons Attribution-NonCommercial 3.0 Unported Licence.

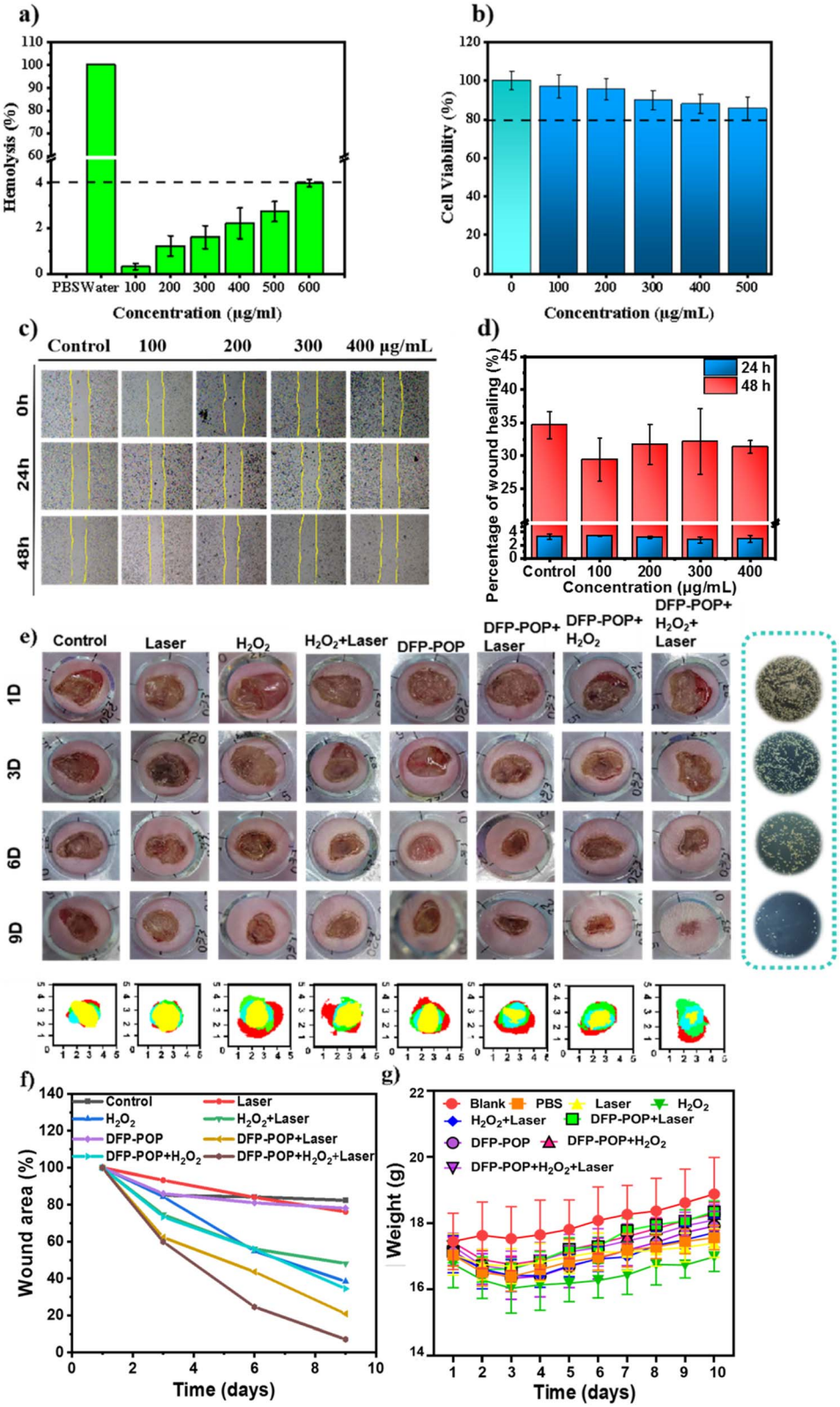

Fig. 8 (a) Hemolysis plots of DFP-POP; (b) MTT assay of L929 after various treatments; (c) cell migration detected by wound healing assay; (d) the statistical graph of corresponding cell migration rate; (e) wound changes of mice with different treatments; (f) daily ratio of wound healing during treatment to wound area on the first day; (g) plot of the daily body weight changes of the mice during the treatment period. Results are presented as mean ± S.D. (*$p < 0.05$, **$p < 0.01$, ***$p < 0.001$, ****$p < 0.0001$, analyzed by Student's t-test).

Open Access Article. Published on 11 December 2025. Downloaded on 3/15/2026 8:19:21 PM.
This article is licensed under a Creative Commons Attribution-NonCommercial 3.0 Unported Licence.

Therapeutic efficacy was then evaluated in back *S. aureus*-infected mouse models using eight treatment groups (PBS, H_2O_2, DFP-POP, DFP-POP + H_2O_2, PBS + laser, H_2O_2 + laser, DFP-POP + laser, and DFP-POP + H_2O_2 + laser). All the animal experiments performed were in strict compliance with the ethical norms of Shandong Second Medical University. Fig. 8e showed the longitudinal wound photographs at days 1, 3, 6, and 9 post-treatment. All groups exhibited progressive wound area reduction over time, though therapeutic efficacy varied substantially. After 9 days, control groups (PBS, PBS + laser, H_2O_2, H_2O_2 + laser) and DFP-POP monotherapy showed negligible healing *versus* baseline. In stark contrast, the phototherapy (DFP-POP + laser) and enzyme therapy (DFP-POP + H_2O_2) group achieved 79.15% and 65.53% wound closure. The combinatorial therapy (DFP-POP + H_2O_2 + laser) demonstrated near-complete healing (92.87% closure). Infrared thermography confirmed effective *in vivo* photothermal conversion, showing sustained temperature elevation during 10 min irradiation cycles (Fig. S16). Bacterial load quantification revealed treatment-dependent clearance. Specifically, the swab samples

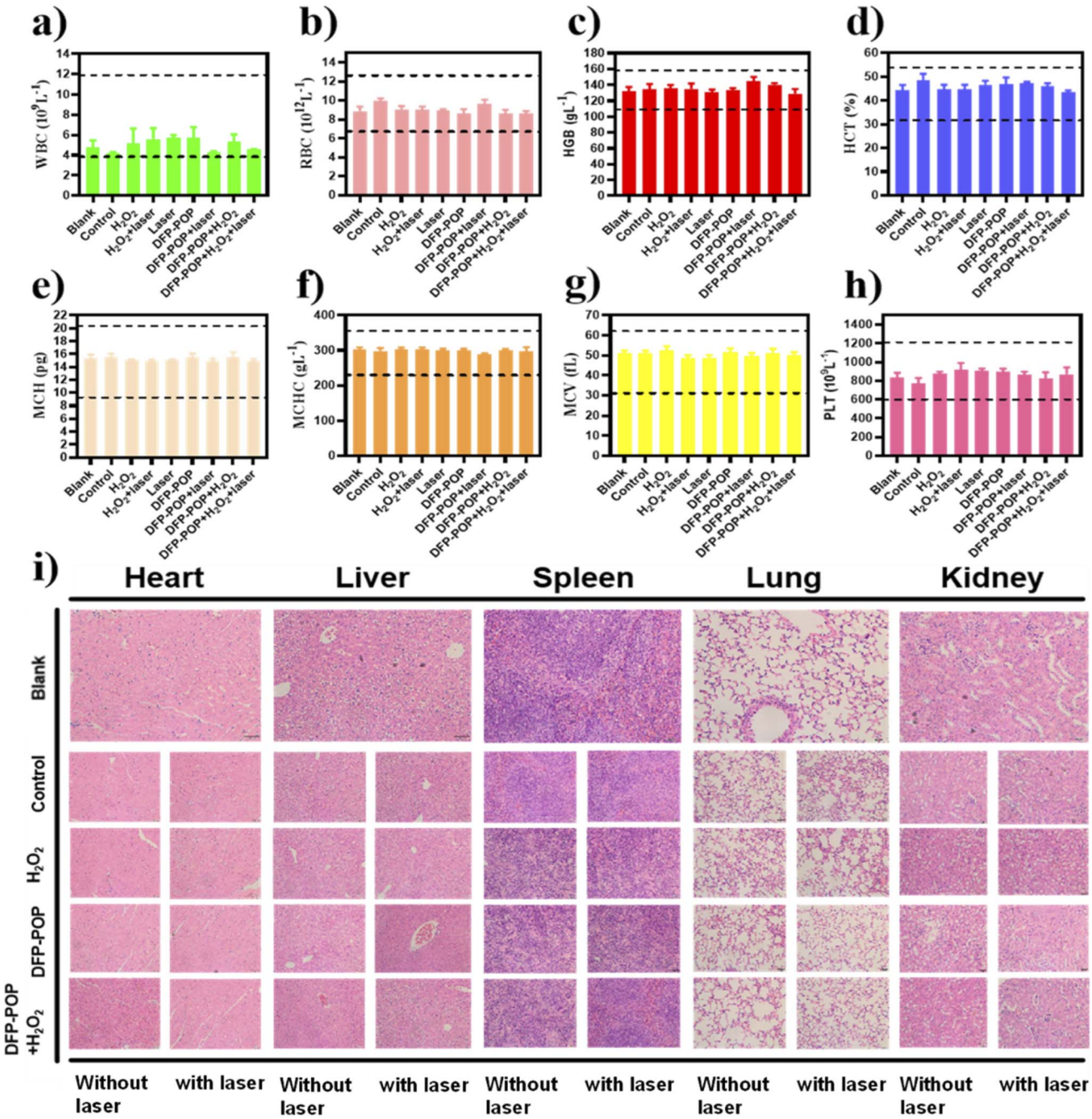

Fig. 9 The biochemical index and histological analysis. (a–h) Routine blood tests in mice on day 9; (i) H&E staining of heart, liver, spleen, lung and kidney of mice after different group. Results are presented as mean ± S.D. (*p < 0.05, **p < 0.01, ***p < 0.001, ****p < 0.0001, analyzed by Student's t-test).

 © 2025 The Author(s). Published by the Royal Society of Chemistry

Open Access Article. Published on 11 December 2025. Downloaded on 3/15/2026 8:19:21 PM.
This article is licensed under a Creative Commons Attribution-NonCommercial 3.0 Unported Licence.

cultured in LB broth showed colony counts decreasing linearly with treatment duration.[52] By day 9, combinatorial therapy achieved complete bacterial eradication. Statistical analysis of the body weight trajectories in Fig. 8g confirmed that all treatment groups maintained stable weights with no significant fluctuations, demonstrating the minimal systemic toxicity of the therapy. Histological analysis (H&E staining, Fig. S17) evaluated *S. aureus*-infected skin regeneration after 9 days of treatment. All groups exhibited varying degrees of angiogenesis and epithelialization, with hierarchical outcomes. The DFP-POP + H_2O_2 + laser group displayed an extensive neovascularization and complete re-epithelialization. The DFP-POP group showed moderate tissue regeneration, significantly enhanced by laser irradiation or H_2O_2 (DFP-POP + H_2O_2 and the DFP-POP + laser). DFP-POP-free groups demonstrated minimal regeneration regardless of illumination. These findings confirm DFP-POP orchestrated a therapeutic cascade for the concurrent PTT ablation, PDT-mediated ROS generation, and POD/CAT enzyme catalysis, realizing microenvironment modulation, thereby synergistically accelerating tissue regeneration.

Finally, comprehensive biocompatibility assessment was performed after 9 days of treatment (Fig. 9). Hematological parameters, including neutrophils and white blood cells (WBCs), were all remained within normal physiological ranges across all groups, with no statistically significant differences *versus* PBS controls (Fig. 9a–h).[53] Histopathological analysis of major organs (heart, liver, spleen, lungs, kidneys) similarly revealed no evidence of tissue damage or morphological abnormalities with identical architecture to untreated controls. These collective findings confirmed the excellent *in vivo* biosafety profile of DFP-POP, demonstrating no significant impact on hematological homeostasis or organ function.

Conclusion

In summary, we have developed a spatial interleaving and twisting strategy that enables targeted engineering of porous organic polymers (POPs) with programmable photophysical properties. This approach maximizes photoactivity while effectively suppressing quenching effects. Through rational structural design, we obtained DFP-POP with spatially optimized, fully conjugated framework that integrates self-enhanced PTT, PDT, as well as CAT- and POD-like activities for synergistic wound treatment. Importantly, DFP-POP dynamically remodels the infectious microenvironment. Specifically, its CAT-mimetic activity converts overexpressed H_2O_2 into O_2, to alleviate hypoxia and potentiate PDT, while its photothermally amplified POD-like activity generates $^{\bullet}OH$. The unique spatial configuration and nanoporous confinement effect together enhance the localized production of reactive oxygen species (ROS), including singlet $^1O_2$ and $^{\bullet}OH$, thereby promoting targeted bacterial membrane disruption. Through this spatially coordinated and dynamically responsive action, DFP-POP effectively eliminates pathogens *via* membrane-disruptive ROS cascades and significantly accelerates tissue regeneration. Thus, DFP-POP functions as a self-sustaining, oxygen-economizing nanozyme that overcomes key limitations of conventional PDT. This work establishes a new paradigm for integrating phototherapeutic and enzyme-mimetic functionalities *via* rational nanoarchitectonics. Looking forward, the proposed spatial engineering strategy and the versatile performance of DFP-POP could be extended to other biomedical applications, such as cancer therapy and biosensing. However, the current findings are primarily based on *in vitro* and preliminary *in vivo* evidence; further long-term toxicological studies, detailed mechanistic investigations, and scalability assessments will be essential to advance its clinical translation.

Ethical statement

All animal procedures were performed in accordance with the Guidelines for Care and Use of Laboratory Animals of Shandong Second Medical University and approved by the Animal Ethics Committee of Shandong Second Medical University.

Author contributions

Meiyun Du, conceptualization. Zongpeng Zhang, methodology. Feng Gao, formal analysis. Yonglei Qin, supervision and administration. Fei Gao, supervision and administration. Peng Sun, writing – original draft, view & editing.

Conflicts of interest

There are no conflicts to declare.

Data availability

All supporting data, including experimental details and characterization files, are included in the manuscript or supplementary information (SI). Supplementary information is available. See DOI: https://doi.org/10.1039/d5ra07169k.

Acknowledgements

This work was supported by the Natural Science Foundation of Shandong Province (ZR2025QC124), Shandong Medical and Health Science and Technology Project (202405020681).

References

1 S. P. Abinaya, J. N. Craig, M. T. Khoa, M. Marco, K. Udit, W. Fei, K. Elayaraja, A. Andrew, D. Christina, H. Megan, Y. Shibu, S. Sudipta and J. C. Melanie, A neoteric antibacterial ceria-silver nanozyme for abiotic surfaces, *Biomaterials*, 2024, **307**, 122527.

2 Y. Sun, W. Zhang, Z. Luo, C. Zhu, Y. Zhang, Z. Shu, C. Shen, X. Yao, Y. Wang and X. Wang, ZnO-CuS/F127 hydrogels with multienzyme properties for implant-related infection therapy by inhibiting bacterial arginine biosynthesis and promoting tissue repair, *Adv. Funct. Mater.*, 2025, **35**(8), 2415778.

3 W. Zheng, W. Sun and A. Simeonov, Drug repurposing screens and synergistic drug-combinations for infectious diseases, *Br. J. Pharmacol.*, 2018, **175**, 181–191.

Open Access Article. Published on 11 December 2025. Downloaded on 3/15/2026 8:19:21 PM.
This article is licensed under a Creative Commons Attribution-NonCommercial 3.0 Unported Licence.

4 P. Chen, R. Ze, X. Xia, Z. Zhang, K. Lu, L. Wei and B. Zhou, Composite porphyrin-based conjugated microporous polymer/graphene oxide capable of photo-triggered combinational antibacterial therapy and wound healing, *Biomater. Adv.*, 2023, **154**, 213662.
5 Z. Pan, Y. Fum, C. Peng, L. Xiao, S. Z, F. Peng, Q. Liu and B. Zhou, Triazine-Porphyrin-based aminal linked porous organic polymer as self-enhanced photo/enzyme synergistic antibacterial agent for wound healing, *Microporous Mesoporous Mater.*, 2024, **365**, 112881.
6 Z. Zhang, L. Shi, L. Chu, P. Chen, P. Sun, Z. Chen, L. Wei and B. Zhou, Crown ether-based porous organic polymer encapsulated $Ag_2[Fe(CN)_5NO]$ composite towards ultra-low dose efficient sterilization and wound healing application, *Mater. Today Chem.*, 2023, **34**, 101794.
7 Z. Hu, J. Shan, X. Jin, W. Sun, L. Cheng, X. Chen and X. Wang, Nanoarchitectonics of in situ antibiotic-releasing acicular nanozymes for targeting and inducing cuproptosis-like death to eliminate drug-resistant bacteria, *ACS Nano*, 2024, **18**(35), 24327–24349.
8 L. Yang, S. Song, M. Yin, M. Yang, D. Yan, X. Wan, J. Xiao, Y. Jiang, Y. Yao and J. Luo, Antibiotic-based small molecular micelles combined with photodynamic therapy for bacterial infections, *Asian J. Pharm. Sci.*, 2023, **18**, 58–69.
9 W. Wang, Y. Cui, X. Wei, Y. Zang, X. Chen, L. Cheng and X. Wang, $CuCo_2O_4$ nanoflowers with multiple enzyme activities for treating bacterium-infected wounds via cuproptosis-like death, *ACS Nano*, 2024, **18**(24), 15845–15863.
10 X. Feng, Z. Luo, W. Zhang, R. Wan, Y. Chen, F. Li, Y. He, Z. Lin, J. H. Hui, J. Conde, S. Chen, Z. Zhao and X. Wang, Zn-DHM Nanozymes Enhance Muscle Regeneration Through ROS Scavenging and Macrophage Polarization in Volumetric Muscle Loss Revealed by Single-Cell Profiling, *Adv. Funct. Mater.*, 2025, **35**, 2506476.
11 Y. Dong, J. Liu, Y. Chen, T. Zhu, Y. Li, C. Zhang, X. Zeng, Q. Chen and Q. Peng, Photothermal and natural activity-based synergistic antibacterial effects of Ti_3C_2Tx MXene-loaded chitosan hydrogel against methicillin-resistant Staphylococcus aureus, *Int. J. Biol. Macromol.*, 2023, **240**, 124482.
12 L. Jiang, C. R. R. Gan, J. Gao and X. J. Loh, A Perspective on the Trends and Challenges Facing Porphyrin-Based Anti-Microbial Materials, *Small*, 2016, **12**, 3609–3644.
13 S. Gai, G. Yang, P. Yang, F. He, J. Lin, D. Jin and B. Xing, Recent advances in functional nanomaterials for light-triggered cancer therapy, *Nano Today*, 2018, **19**, 146–187.
14 Z. Meng, W. Hou, H. Zhou, L. Zhou, H. Chen and C. Wu, Therapeutic Considerations and Conjugated Polymer-Based Photosensitizers for Photodynamic Therapy, *Macromol. Rapid Commun.*, 2018, **39**, 1700614.
15 Y. Sun, R. Ogawa, B. H. Xiao, Y. X. Feng, Y. Wu, L. H. Chen, X. H. Gao and H. D. Chen, Antimicrobial photodynamic therapy in skin wound healing: A systematic review of animal studies, *Int. Wound J.*, 2020, **17**(2), 285–299.
16 P. Chen, J. Wang, X. Feng, K. Li, Q. Liu, L. Ji, H. Li, P. Sun, J. Li and B. Zhou, Bidirectionally regulated synthetic ferrocene-based aminal-linked porous organic polymer artificial enzyme towards photothermal-amplified synergistic antibacterial and wound healing therapy, *Polym. Test.*, 2024, **135**, 108466.
17 R. Zhang, X. Yan, L. Gao and K. Fan, Nanozymes expanding the boundaries of biocatalysis, *Nat. Commun.*, 2025, **16**(1), 6817.
18 X. Fan, X. Fu, S. Han, D. Sun, R. Wang, M. Zhang, W. Jiang and K. Fan, Stimuli-responsive nanozymes in imaging and therapy of critical diseases, *Coord. Chem. Rev.*, 2026, **546**, 217033.
19 S. Zhang, R. Xu, S. He, R. Sun, G. Wang, S. Wei, X. Yan and K. Fan, Nanozyme-driven multifunctional dressings: moving beyond enzyme-like catalysis in chronic wound treatment, *Mil. Med. Res.*, 2025, **12**, 27.
20 D. Li, Y. Fang and X. Zhang, Bacterial Detection and Elimination Using a Dual-Functional Porphyrin-Based Porous Organic Polymer with Peroxidase-Like and High Near-Infrared-Light-Enhanced Antibacterial Activity, *ACS Appl. Mater. Interfaces*, 2020, **12**, 8989–8999.
21 M. Overchuk, R. A. Weersink, B. C. Wilson and G. Zheng, Photodynamic and Photothermal Therapies: Synergy Opportunities for Nanomedicine, *ACS Nano*, 2023, **17**, 7979–8003.
22 W. Guo, H. Ren, Y. Jin, Z. Chai and B. Liu, The bioremediation of the typical persistent organic pollutants (POPs) by microalgae-bacteria consortia: A systematic review, *Chemosphere*, 2024, **355**, 141852.
23 P. Gao, X. Shen, X. Liu, B. Cui, M. Wang, X. Wan, N. Li and B. Tang, Covalent organic framework-derived carbonous nanoprobes for cancer cell imaging, *ACS Appl. Mater. Interfaces*, 2021, **13**(35), 41498–41506.
24 Y. Zhang and S. N. Riduana, Functional porous organic polymers for heterogeneous catalysis, *Chem. Soc. Rev.*, 2012, **41**, 2083–2094.
25 Y. Zhu, P. Xu, X. Zhang and D. Wu, Emerging porous organic polymers for biomedical applications, *Chem. Soc. Rev.*, 2022, **51**, 1377–1414.
26 A. Singh, R. Gogoi, K. Sharma, S. K. Jena, N. Fourati, C. Zerrouki, S. Remita and P. F. Siril, Continuous flow synthesis of visible light-active conjugated porous polymer for pollutant degradation and plastic waste photoreforming, *J. Cleaner Prod.*, 2023, **428**, 139476.
27 H. Kaur, S. S. Siwal, R. V. Saini and V. K. Thakur, Covalent–Organic Framework-Based Materials in Theranostic Applications: Insights into Their Advantages and Challenges, *ACS Omega*, 2024, **9**, 6235–6252.
28 J. W. Maina, J. A. Schütz, L. Grundy, L. E. Des, Z. Yi, L. Kong, C. Pozo-Gonzalo, M. Ionescu and L. F. Dumée, Inorganic Nanoparticles/Metal Organic Framework Hybrid Membrane Reactors for Efficient Photocatalytic Conversion of CO_2, *ACS Appl. Mater. Interfaces*, 2017, **9**, 35010–35017.
29 Z. Chen, X. Li, C. Yang, K. Cheng, T. Tan, Y. Lv and Y. Liu, Hybrid Porous Crystalline Materials from Metal Organic Frameworks and Covalent Organic Frameworks, *Adv. Sci.*, 2021, **8**, e2101883.
30 J. He, Y. Wang, J. Yuan, C. Liu, C. Pan, Z. Weng, X. Tang, Y. Liu and G. Yu, Ferrocene-integrated conjugated

 © 2025 The Author(s). Published by the Royal Society of Chemistry

Open Access Article. Published on 11 December 2025. Downloaded on 3/15/2026 8:19:21 PM. This article is licensed under a Creative Commons Attribution-NonCommercial 3.0 Unported Licence.

microporous polymer nanosheets: Active and regenerative catalysts for photomediated controlled radical polymerization, *Appl. Mater. Today*, 2020, **18**, 100507.

31 B. Traoré, N. Diouf, M. Kébé, R. Guéye-Sylla, I. E. Thiam, O. Diouf, P. Retailleau and M. Gaye, Crystal structure of poly[hexa-μ-bro-mido-bis{2-[1-(py-ri-din-2-yl)ethyl-idene-amino]ethanol-ato}tetracopper(II)], *Acta Crystallogr., Sect. E: Crystallogr. Commun.*, 2024, **80**, 133–136.

32 Z. Zong, Y. Kimura, M. Takahashi and H. Yamane, Characterization of chemical and solid state structures of acylated chitosans, *Polymer*, 2000, **41**, 899–906.

33 Y. Yang, M. Ishidam, Y. Yasutake, S. Fukatsu, C. Fukakusa, M. Morikawa, Y. Teppei, N. Kimizuka and H. Furuta, Hierarchical hybrid metal–organic frameworks: tuning the visible/near-infrared optical properties by a combination of porphyrin and its isomer units, *Inorg. Chem.*, 2019, **58**, 4647–4656.

34 W. Zhang, C. Li, Y. Yuan, L. Qiu, A. Xie, Y. Shen and J. Zhu, Highly energy- and time-efficient synthesis of porous triazine-based framework: microwave-enhanced ionothermal polymerization and hydrogen uptake, *J. Mater. Chem.*, 2010, **20**, 6413–6415.

35 J. P. Denis and J. Gagnon, Determination of the degree of quaternization of *N*,*N*,*N*-trimethylchitosan by CP-MAS ^{13}C NMR, *Carbohydr. Res.*, 2023, **523**, 108736.

36 Z. F. Pang, T. Y. Zhou, R. R. Liang, Q. Y. Qi and X. Zhao, Regulating the topology of 2D covalent organic frameworks by the rational introduction of substituents, *Chem. Sci.*, 2017, **8**, 3866–3870.

37 C. Miao, N. Tang, L. Shi, S. Wang, P. Ji, J. Zhang, Z. Wang and B. Zhou, Ionic Functionalized Magnetic Porous Polymers as Advanced Materials for High-Efficiency Water Decontamination: Bactericidal and Iodine Adsorption, *ACS Appl. Polym. Mater.*, 2023, **5**, 8679–8692.

38 Z. Guo, H. Jiang, H. Wu, L. Zhang, S. Song, Y. Chen, C. Zheng, Y. Ren, R. Zhao, Y. Li, Y. Yin, M. D. Guiver and Z. Jiang, Oil–water–oil triphase synthesis of ionic covalent organic framework nanosheets, *Angew. Chem., Int. Ed.*, 2021, **133**, 27284–27291.

39 M. Zhang, F. Yan, J. Bai, X. Li, X. Zheng, J. Dou, X. Wang, W. Zhang and B. Zhou, ZIF-67-templated synthesis of core-shell-structured POP@MOF composite derived porous carbon with embedding FeCo alloy nanoparticles as high-performance bifunctional oxygen electrocatalysts, *Microporous Mesoporous Mater.*, 2021, **312**, 110627.

40 S. Drouet, A. Merhi, D. Yao, M. P. Cifuentes, M. G. Humphrey, M. Wielgus, B. J. Olesiak, K. Matczyszyn, M. Samoc, F. Paul and C. O. Paul-Roth, Cubic nonlinear optical properties of new zinc tetraphenyl porphyrins peripherally functionalized with electron-rich Ru(II) alkynyl substituents, *Tetrahedron*, 2012, **68**(50), 10351–10359.

41 H. Shi, C. Xiong, L. Zhang, H. Cao, R. Wang, P. Pan, H. Guo and T. Liu, Light-Triggered Nitric Oxide Nanogenerator with High L-Arginine Loading for Synergistic Photodynamic/Gas/Photothermal Therapy, *Adv. Healthcare Mater.*, 2023, **12**, e2300012.

42 Y. Li, X. Liu, L. Tan, Z. Cui, X. Yang, Y. Zheng, K. Wai, K. Yeung, K. C. Paul and S. Wu, Rapid Sterilization and Accelerated Wound Healing Using Zn^{2+} and Graphene Oxide Modified g-C_3N_4 under Dual Light Irradiation, *Adv. Funct. Mater.*, 2018, **28**, 0299.

43 A. Lanzilotto, M. Kyropoulou, E. C. Constable, C. E. Housecroft, W. P. Meier and C. G. Palivan, Porphyrin-polymer nanocompartments: singlet oxygen generation and antimicrobial activity, *J. Biol. Inorg. Chem.*, 2018, **23**, 109–122.

44 Q. Chen, C. Wang, C. Liang and Z. Liu, Near-infrared dye bound human serum albumin with separated imaging and therapy wavelength channels for imaging-guided photothermal therapy preventing tumor metastasis, *J. Controlled Release*, 2015, **213**, e89.

45 X. Dou, Z. Lin, H. Chen, Y. Zheng, C. Lu and J. Lin, Production of superoxide anion radicals as evidence for carbon nanodots acting as electron donors by the chemiluminescence method, *Chem. Commun.*, 2013, **49**, 5871–5873.

46 F. Yu, Y. Xiao and L. Tao, The activation of PMS for PFOA degradation by adjustable metal stripping Fe/Co/N@BC catalysts: Degradation performance with single-line oxygen and high-valent metal oxides as the main active substances, *Sep. Purif. Technol.*, 2024, **351**, 127589.

47 Z. Gao, Y. Li, Y. Zhang, K. Cheng, P. An, F. Chen, J. Chen, C. You, Q. Zhu and B. Sun, Biomimetic Platinum Nanozyme Immobilized on 2D Metal-Organic Frameworks for Mitochondrion-Targeting and Oxygen Self-Supply Photodynamic Therapy, *ACS Appl. Mater. Interfaces*, 2020, **12**(2), 1963–1972.

48 M. R. J. Salton, Studies of the bacterial cell wall: IV. The composition of the cell walls of some Gram-positive and Gram-negative bacteria, *Biochim. Biophys. Acta*, 1953, **10**, 512–523.

49 P. Gao, X. Shen, X. Liu, B. Cui, M. Wang, X. Wan, N. Li and B. Tang, Covalent Organic Framework-Derived Carbonous Nanoprobes for Cancer Cell Imaging, *ACS Appl. Mater. Interfaces*, 2021, **13**(35), 41498–41506.

50 L. Mei, Z. Xu, Z. Miao, M. Yun, Y. Luan, D. Yang and L. Xia, Polymyxin B-functionalized phthalocyanine for chemo-photodynamic antibacterial therapy in enhanced wound healing dagger, *New J. Chem.*, 2021, **45**, 6450–6457.

51 Y. Jia, L. Zhang, B. He, Y. Lin, J. Wang and M. Li, 8-Hydroxyquinoline functionalized covalent organic framework as a pH sensitive carrier for drug delivery, *Mater. Sci. Eng., C*, 2020, **117**, 111243.

52 B. Liu, Y. Su, S. Wu and J. Shen, Local Photothermal/Photodynamic Synergistic Antibacterial Therapy Based on Two-dimensional BP@CQDs Triggered by Single NIR Light Source, *Photodiagn. Photodyn. Ther.*, 2022, **39**, 102905.

53 Y. Zhao, A. X, P. Wu, F. Chen, Q. Zhang, X. Liang, X. Han, X. Shi, Y. Li and Y. Chen, Fabrication of Hydroxypropyl Chitosan/Soy Protein Isolate Hydrogel for Effective Hemorrhage Control, *Tissue Eng., Part A*, 2020, **27**, 788–795.